THE JOURNAL OF PHYSICAL CHEMISTRY C

Article

Cite This: J. Phys. Chem. C 2018, 122, 28158−28172

pubs.acs.org/JPCC

Understanding Surface Catalyzed Decomposition Reactions Using a Chemical Pathway Analysis

Robert H. Wells,[†] Xiang-Kui Gu,[‡] Wei-Xue Li,*[,§] and Rex T. Skodje*[,†]

[†]Department of Chemistry, University of Colorado, Boulder, Colorado 80309-0215, United States

[‡]Department of Chemical Engineering and Materials Science, Wayne State University, Detroit, Michigan 48202, United States

[§]Department of Chemical Physics, School of Chemistry and Materials Science, iChEM, CAS Center for Excellence in Nanoscience, Hefei National Laboratory for Physical Sciences at the Microscale, University of Science and Technology of China, Hefei 230026, China

Supporting Information

ABSTRACT: A theoretical microkinetic model is developed to describe the decomposition of methanol into formaldehyde, carbon monoxide, and hydrogen on eight transition metal surfaces using density functional theory (DFT) calculations and transition state theory (TST). The chemical kinetics are then analyzed using a recently developed technique, the sum over histories representation (SOHR), that clearly reveals the chemical pathways followed by the system. The model itself consists of 10 reversible hydrogen abstraction reactions as well as the adsorption−desorption of methanol, formaldehyde, hydrogen, and carbon monoxide. The computed rate coefficients are fit to generalized Arrhenius expressions that are applicable to a wide range of conditions. While the lateral interactions are not explicitly computed, the effects of surface coverage are included using a site-blocking model for the kinetics. The SOHR method allows the chemical pathways followed by the surface species to be determined and weighted by unique probabilities. Locating the most probable chemical pathways is very useful in understanding the selectivity of product formation and can be used to determine the "optimal" reaction conditions.

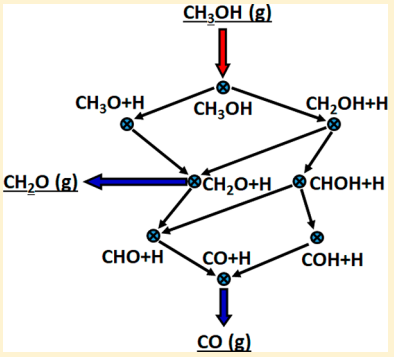

I. INTRODUCTION

It is a long-standing goal to develop a molecular level understanding of the chemical kinetics that underlie complex surface catalytic processes for heterogeneous reactions.[1,2] The detailed chemistry of catalytic mechanisms is responsible for the behavior of macroscopic observables such as turnover frequency and product selectivity. Since many of the elementary processes and reaction intermediates involved in complex mechanisms are not presently accessible to experimental observation, researchers have relied on theoretical calculations to elucidate the details of many catalytic systems.[3] Recent theoretical advances including the use of density functional theory (DFT), kinetic Monte Carlo methods, and mean field methods can allow quantitative prediction of catalytic activity.[4−7] The present work consists of a sequence of two interconnected components. First, a microkinetic model is developed for the decomposition kinetics of methanol on eight transition metal surfaces. The barrier energies and vibrational frequencies are obtained using a density functional theory (DFT) approach, and the rate coefficients are obtained from transition state theory (TST). While lateral interactions are not computed, the role of surface coverage is included using a site-blocking model for the chemical kinetics whereby dissociation into an occupied site is forbidden. The second component of this work investigates the kinetic behavior using a newly developed sum over histories representation (SOHR) method[8−11] that emphasizes the global kinetics through its formulation in terms of complete chemical pathways which follow molecules from reagents to products. Using these techniques, we aim to develop new insight into kinetic behavior of catalytic surface reactions.

One approach that is commonly used to decipher the chemistry of complex surface catalysis mechanisms is to delineate the reaction pathways leading from reagents to products.[12−14] These pathways follow a chemical moiety from reagent to product states through a series of intermediates species which are connected by transition states. The notion of the reaction pathway is ubiquitous in chemistry and is routinely used in problems ranging from chemical synthesis to combustion kinetics. In catalysis, a dominant pathway (i.e., the most probable pathway) provides a *de facto* reaction mechanism and hence identifies the key reaction steps and intermediates en route to products. A dominant pathway can provide simple means to interpret the rate parameters for the turnover frequency (such as its activation energy) and provides a guide to optimizing the choice of catalysts. Unfortunately, the use of pathway analysis becomes confusing when the reaction network grows large and can support numerous contributing

Received: September 26, 2018
Revised: November 13, 2018
Published: November 14, 2018

DOI: 10.1021/acs.jpcc.8b09415
J. Phys. Chem. C 2018, 122, 28158−28172

Table 1. Most Stable Binding Energies (in eV) of the Intermediates Involved in Methanol Dehydrogenation on Eight Surfaces[a]

	Rh(111)	Ir(111)	Cu(111)	Au(111)	Ag(111)	Pd(111)	Pt(111)	Ni(111)
CH_3OH	−0.32 (−0.28)	−0.3 (0.26)	−0.17 (−0.15)	−0.13 (−0.11)	−0.14 (−0.12)	−0.25 (−0.22)	−0.59 (−0.55)	−0.25 (−0.22)
CH_3O	−2.33	−1.99	−2.45	−1.38	−1.91	−1.99	−1.48	−2.66
CH_2OH	−1.96	−1.96	−1.11	−1.30	−0.81	−1.88	−2.08	−1.65
CH_2O	−0.91 (−0.83)	−0.64 (−0.54)	−0.18 (−0.13)	−0.04 (−0.03)	−0.03 (−0.02)	−0.64 (−0.57)	−0.72 (−0.65)	−0.82 (−0.75)
HCOH	−3.22	−3.38	−2.05	−2.02	−1.40	−3.26	−3.39	−2.97
HCO	−2.55	−2.37	−1.41	−1.44	−0.98	−2.51	−2.44	−2.35
COH	−4.69	−4.65	−2.99	−2.72	−1.84	−4.68	−4.71	−4.50
CO	−1.45 (−1.4)	−1.58 (−1.54)	−0.5 (−0.46)	−0.4 (−0.36)	−0.28 (−0.25)	−1.48 (−1.42)	−1.35 (−1.3)	−1.28 (−1.24)
H	−2.81	−2.68	−2.53	−2.25	−2.13	−2.94	−2.76	−2.86

[a]The quantities in parentheses are the zero-point corrected adsorption energies.

paths.[15−21] Furthermore, the use of simplistic notions of reaction paths based on lowest reaction barriers can fail badly should entropic or quantum effects become important. Our recently developed quantitative theory of chemical pathways, i.e., the SOHR method, allows us to overcome many of these shortcomings by providing a rigorous and numerically convergent theory of chemical pathways.[8−11] Using an approach motivated by Feynman's path integral representation for quantum mechanics,[22] the kinetics of a general nonlinear and nonstationary chemical mechanism are quantitatively represented by an expansion in chemical pathways. The concentrations for species $\{S_1, ..., S_n\}$, i.e., $\mathbf{X}(t) = \{X_1(t), ..., X_n(t)\}$, can be expressed as a pathway expansion of the chemical propagator $\boldsymbol{T}$ as

$$\mathbf{X}(t) = \mathbf{T}(t_0, t)\cdot\mathbf{X}(t_0) \tag{1.1}$$

$$T_{j(i,k)}(t_0, t) = \sum_{j(i,k)} c_{j(i,k)} P_j(t) \tag{1.2}$$

where $j(i, k)$ indicates chemical pathways linking the initial species S_i to the final species S_k, $P_j(t)$ are the associated probabilities of those paths, and c_j are trivial stoichiometric coefficients. The details of the pathway expansion are reviewed below and discussed in detail in refs 8−12. We have shown that many aspects of a kinetic model, such as the sensitivity coefficients and arrival time distributions, can be understood using SOHR.

We shall consider the catalytic decomposition of methanol (MeOH) on eight transition metal surfaces, viz., the (111) surface of Pt, Pd, Ir, Ru, Ag, Au, Cu, and Ni. The decomposition process has two possible product channels:

$$CH_3OH(g) \rightarrow CO(g) + 2H_2(g)$$

$$\Delta G(T = 800\ \text{K}) = -85.0\ \text{kJ/mol}$$

$$CH_3OH(g) \rightarrow CH_2O(g) + H_2(g)$$

$$\Delta G(T = 800\ \text{K}) = 4.6\ \text{kJ/mol}$$

The product selectivity of the reaction is an important observable. Methanol decomposition is potentially useful for H_2 production[23] and is related to numerous important catalytic systems, such as methanol steam reforming,[24−28] methanol partial oxidation,[29−31] methanol electro-oxidation,[32−34] and methanol synthesis.[35−64] The system has also been crucial for developing empirical methods such as linear scaling relationships to simplify energetic calculations on surfaces.[65−70] While the eight metals are modeled using the same elementary processes in the microkinetic model, the controlling chemical pathways are found to be quite different. This systematic study provides a comprehensive test for the ability of the SOHR method to predict reactions routes as a function of reactor condition and catalytic metal.

In Section II, the theoretical methods used in this study are introduced. The DFT calculations used to locate the transition state structures are discussed in Section II.A. The microkinetic model is presented in Section II.B, and the associated rate coefficients are computed using the TST methods discussed in Section II.C. The SOHR methodology is briefly reviewed in Section II.D. The chemical pathways followed by the methanol molecules are enumerated in Section III. A simple "forward-only" model based on a subset of these pathways is also presented. In Section IV, the results are presented and discussed. The energy landscapes for all eight metals are shown, and the rate coefficients for all the processes are determined. The exact pathway probabilities as functions of reactor temperature and pressure are obtained. The forward-only model is found to be very accurate at low surface coverage but can show some significant error at high coverage. It is found that the kinetics on the eight metals are quite different from one to another and follow distinct reaction routes. The cases of Pd(111) and Ir(111) are considered in detail. It is found that the reaction pathways followed by the system are strong functions of temperature and pressure which can be physically understood from the behavior of the system at four key branching points of the surface kinetics. Finally, Section V presents the conclusions of this work.

II. THEORETICAL METHODS

II.A. Density Functional Theory Calculations. Periodic DFT calculations were performed using the Vienna *ab initio* Simulation Package (VASP).[71,72] The exchange-correlation interaction is described by the generalized gradient approximation (GGA) and PW91 functional.[73] The Kohn−Sham equations were solved by using a plane-wave basis set with a kinetic energy cutoff of 400 eV. The (111) surfaces of Pd, Pt, Rh, Ir, Ni, Cu, Au, and Ag are modeled with a four-layer slab model with a (3 × 3) unit cell. A (5 × 5 × 1) k-point mesh is used to sample the surface Brillouin zone, and a 12 Å vacuum is introduced between the repeated slabs along the *z*-direction. During optimization, the bottom two layers of the slab are fixed, while the remaining atoms and adsorbates are relaxed until the residual forces are less than 0.05 eV/Å. The transition state (TS) of the elementary step is determined using the climbing-image nudged elastic band (CI-NEB) method.[74,75] The vibrational frequencies were calculated for the equilibrium and transition state structures by diagonalizing the force constant matrix, including only the adsorbate degrees of freedom, obtained from finite differences of the potential

DOI: 10.1021/acs.jpcc.8b09415
J. Phys. Chem. C 2018, 122, 28158−28172

Table 2. Barrier Energies (in eV) for the Reactions in the Microkinetic Model[a]

	Rh(111)			Ir(111)			Cu(111)			Au(111)		
reaction	$E_{forward}$	E_{zpc}	$E_{reverse}$	$E_{forward}$	E_{zpc}	$E_{reverse}$	$E_{forward}$	E_{zpc}	$E_{reverse}$	$E_{forward}$	E_{zpc}	$E_{reverse}$
(0) $CH_3OH(g) + * \rightarrow CH_3OH*$	0		0.32	0		0.30	0		0.17	0		0.13
(1) $CH_3OH* + * \rightarrow CH_3O* + H*$	0.76	0.54	0.88	0.70	0.50	0.37	1.07	0.86	1.18	1.78	1.56	0.58
(2) $CH_3O* + * \rightarrow CH_2O* + H*$	0.53	0.37	0.74	0.44	0.33	0.63	1.27	1.07	0.35	0.71	0.52	0.44
(3) $CH_2O* + * \rightarrow CHO* + H*$	0.25	0.16	0.70	0.34	0.23	0.71	0.76	0.59	0.52	0.89	0.73	0.54
(4) $CHO* + * \rightarrow CO* + H*$	0.30	0.23	1.35	0.58	0.47	1.72	0.21	0.16	1.09	0.51	0.35	0.62
(5) $CH_3OH* + * \rightarrow CH_2OH* + H*$	0.67	0.50	0.79	0.72	0.56	0.73	1.40	1.22	0.54	1.07	0.94	0.16
(6) $CH_2OH* + * \rightarrow CHOH* + H*$	0.45	0.30	0.67	0.55	0.48	0.63	0.81	0.65	0.43	1.43	1.26	0.55
(7) $CHOH* + * \rightarrow COH* + H*$	0.07	0	0.79	0.19	0.12	0.79	0.76	0.60	0.67	1.52	1.35	0.91
(8) $COH* + * \rightarrow CO* + H*$	0.97	0.79	1.74	1.09	0.91	1.81	1.04	0.84	2.20	1.04	0.85	1.73
(9) $CH_2OH* + * \rightarrow CH_2O* + H*$	0.69	0.46	0.90	0.67	0.48	0.52	0.91	0.69	0.96	0.79	0.57	0.23
(10) $CHOH* + * \rightarrow CHO* + H*$	0.63	0.43	1.07	0.39	0.21	0.56	0.93	0.71	1.12	0.31	0.14	0.46
(11) $H* + H* \rightarrow H_2(g) + 2*$	1.06			0.86			0.89			0.71		
(12) $CH_2O* \rightarrow CH_2O(g) + *$	0.91			0.64			0.18			0.04		
(13) $CO* \rightarrow CO(g) + *$	1.45			1.58			0.50			0.40		
	Pd(111)			Pt(111)			Ni(111)			Ag(111)		
reaction	$E_{forward}$	E_{zpc}	$E_{reverse}$	$E_{forward}$	E_{zpc}	$E_{reverse}$	$E_{forward}$	E_{zpc}	$E_{reverse}$	$E_{forward}$	E_{zpc}	$E_{reverse}$
(0) $CH_3OH(g) + * \rightarrow CH_3OH*$	0		0.25	0		0.20	0		0.25	0	0	0.14
(1) $CH_3OH* + * \rightarrow CH_3O* + H*$	1.07	0.86	1.05	0.81	0.63	0.26	0.78	0.55	1.35	1.58	1.34	0.78
(2) $CH_3O* + * \rightarrow CH_2O* + H*$	0.60	0.43	1.01	0.20	0.06	0.63	0.85	0.68	0.69	1.17	0.96	0.24
(3) $CH_2O* + * \rightarrow CHO* + H*$	0.36	0.19	1.17	0.55	0.40	1.31	0.34	0.19	0.73	1.03	0.89	0.11
(4) $CHO* + * \rightarrow CO* + H*$	0.28	0.18	1.68	0.28	0.16	1.23	0.19	0.13	1.48	0.36	0.19	0.57
(5) $CH_3OH* + * \rightarrow CH_2OH* + H*$	0.55	0.37	0.79	0.62	0.46	0.93	0.74	0.55	0.67	1.92	1.72	0.39
(6) $CH_2OH* + * \rightarrow CHOH* + H*$	0.58	0.42	1.05	0.59	0.42	0.81	0.41	0.24	0.74	1.45	1.25	0.32
(7) $CHOH* + * \rightarrow COH* + H*$	0.38	0.27	1.18	0.57	0.43	1.09	0.06	0	0.89	1.49	1.29	0.50
(8) $COH* + * \rightarrow CO* + H*$	0.83	0.66	1.92	0.91	0.74	1.45	0.96	0.77	1.96	0.92	0.72	2.13
(9) $CH_2OH* + * \rightarrow CH_2O* + H*$	0.69	0.47	0.84	0.81	0.63	0.38	0.62	0.36	1.10	0.97	0.72	0.77
(10) $CHOH* + * \rightarrow CHO* + H*$	0.66	0.45	1.15	0.15	0	0.39	0.65	0.44	1.19	0.57	0.36	0.68
(11) $H* + H* \rightarrow H_2(g) + 2*$	1.29			0.96			1.20			0.75		
(12) $CH_2O* \rightarrow CH_2O(g) + *$	0.64			0.44			0.82			0.03		
(13) $CO* \rightarrow CO(g) + *$	1.48			1.37			1.28			0.28		

[a]Reactions R1−R10 are the hydrogen abstraction reactions shown in Figure 1. Reaction 0 is the methanol adsorption/desorption while reactions 11−13 are for desorption of H_2, CH_2O, and CO, respectively. We defined $E_{forward}$ and $E_{reverse}$ as the classical barrier energies for the forward and reverse reactions, while E_{zpc} refers to the zero-point corrected energies for the forward reactions. We assume that CH_3OH adsorption is a barrierless process. The values for CO desorption are taken from experiment.[83] Negative barrier heights are set to 0.

performed by VASP. The binding energies of the adsorbates and activation energies for the surface reactions are presented in Tables 1 and 2, respectively. The energetics are calculated assuming that lateral interactions between adsorbates are negligible which becomes exact in the limit of zero coverage. It is assumed that H-atom diffusion is rapid, so that the final state products for the H-atom dissociation reactions are spatially isolated.

II.B. Microkinetic Model. The kinetic model for the catalytic dehydrogenation of methanol consists of 14 elementary processes that are graphically represented in Figure 1. The MeOH molecule, CH_3OH, can adsorb and desorb from the gas phase, while the product species CO, H_2, and CH_2O are allowed to desorb only. Once adsorbed, the CH_3OH can undergo a series of reversible H-atom abstraction reactions yielding the adsorbed species CH_3O, CH_2OH, CH_2O, HCOH, CHO, COH, and CO. The forward reactions RH → R + H, labeled R1−R10, are modeled as second-order processes described by second-order rate laws $k_f(T)\theta_{RH}\theta*$ where θ_{RH} is the coverage of species RH and $\theta*$ is the coverage of free sites on the surface.[33,76] Although we do not explicitly include lateral interactions on the surface, the inclusion of free site coverage in the rate laws allows the model to reflect site-blocking effects at sufficiently high pressures. The backward

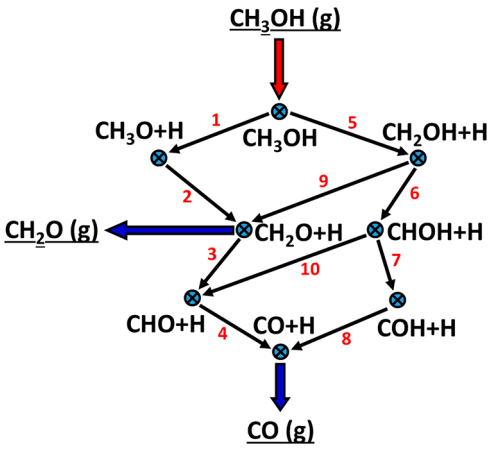

Figure 1. Reaction network for the decomposition of CH_3OH on any of the eight catalytic metals. The CH_3OH, CO, and CH_2O species are allowed to desorb while CH_3OH is also allowed to adsorb to the surface. The reactions 1−10 are dehydrogenation reactions RH → R + H in the forward direction and recombination reactions in the backward direction.

DOI: 10.1021/acs.jpcc.8b09415
J. Phys. Chem. C 2018, 122, 28158−28172

recombination reactions, R + H → RH (BR1−BR10), are described by the rate laws $k_r(T)\theta_R\theta_H$. In the present model, rapid diffusion is assumed to produce homogeneous distributions of each species.

The adsorption of MeOH is assumed to be a first-order process, MeOH(g) + * → MeOH*. The rate law is expressed in terms of the MeOH pressure as $k_a(T)\theta^*$ where $k_a(T) = P_{MeOH}S/N_0\sqrt{2\pi m k_B T}$. The value of the sticking coefficient per site, S/N_0, can be absorbed into an effective value of the pressure of MeOH, and in our simulations we have set $S = 1$. The desorption process is also first-order as described by the rate law, $k_d(T)\theta_X$ with X = MeOH, CO, or CH_2O.

The chemistry of the system is modeled using conventional mass action kinetics where each adsorbed species S_i is characterized by a time-dependent coverage, $\theta_i(t)$, which is assumed to be spatially homogeneous. The time-evolution of the coverages, $\theta_i(t)$, is then obtained using either the differential rate equations or the SOHR expressions presented below.

II.C. Rate Coefficients. The rate coefficients $k(T)$ are computed using data compiled from the DFT calculations. The rates of the abstraction reactions are computed using transition state theory (TST). Thus, the rate coefficient is expressed as[12,77−79]

$$k_{uni}(T) = \left(\frac{k_B T}{h}\right)\left(\frac{N_{TS}}{N_R}\right)\left(\frac{n_{TS}}{n_R}\right)\left(\frac{\sigma_R}{\sigma_{TS}}\right)\frac{Q^0_{TS}}{Q^0_R}e^{-\Delta E_0/k_B T} \tag{2.3}$$

We define ΔE_0 as the zero-point corrected barrier height. The pre-exponential factor is temperature-dependent through the partition functions Q^0_{TS} and Q^0_R, which correspond to the vibrational motion at the TS and reagent, respectively. A normal-mode analysis at the stationary points yields the frequencies for a separable harmonic model but where certain low-frequency modes must employ hindered rotor partition functions. The other terms present in the pre-exponential factor are constant symmetry factors that represent the multiplicity of the TS. We set σ_{TS} and σ_R to be the molecular symmetry number of the TS and reagent, respectively, and n_{TS} and n_R are the number of physically distinct chiral conformations of the TS and reagent. Thus, the quantity $(n_{TS}/n_R)(\sigma_R/\sigma_{TS})$ is identical to the usual symmetry factor for gas phase reactions. The factors N_R and N_{TS} count all possible adsorption sites and molecular orientations within the unit cell for the reagent and TS, respectively. The factor N_{TS}/N_R applied to the rate coefficient can be thought of as roughly the difference in the degeneracy between the TS and the reagent configurations. The rate coefficients for the backward recombination reactions are obtained by microreversibility.

The first-order desorption rate coefficients for CH_3OH, CH_2O, and CO are found using an empirical technique introduced by Campbell et al.[80,81] Assuming that $k_d(T) = \nu \exp(-E_0/k_B T)$, where E_0 is the desorption energy given in Table 1, the prefactor ν is given in terms of the species entropies as

$$\nu = k_B T/h \exp[(S^0_{gas} - S_{gas,1D\text{-}trans} - S_{ad})/R] \tag{2.4}$$

Here, the TS is modeled as a free (gas phase) species with one translational degree of freedom frozen. However, Campbell et al.[81] noted that good agreement with experiment can often be obtained by simply taking the entropy of the adsorbed species to be ∼2/3 that of the gas phase value. This approach should be valid at the temperatures considered here where the adsorbed species are highly mobile. We employed this simple rule to calculate ν. Finally, for the H_2 associative desorption process which possesses a clear saddle-point on the potential energy surface, we employ the TST expression (eq 2.3) with a symmetry factor of unity.

II.D. Sum over Histories Representation. The contributions from detailed molecular pathways that lead to the CH_2O(g) and CO(g) products are quantified using the SOHR method.[8−11] Briefly, the SOHR method represents the kinetics using chemical pathways that follow a tagged-atom as it migrates from species to species due to chemical reactions. The jth pathway probability for a tagged-atom residing in an initial species S_0 at time $t = t_0$ which is delivered to a final species S_n at time t_f through a specific sequence of reactions, $S_0 \underset{R1}{\rightarrow} S_1 \underset{R2}{\rightarrow} S_2 \ldots \underset{Rn}{\rightarrow} S_n$, is denoted by $P_j(t_0, t_f)$. Given the initial species concentrations, the concentration of the final species $[S_n(t_f)]$ is given by linear combination

$$[S_i(t_f)] = \sum_j P_j(t_0, t_f)c_j[S_0(t_0)] \tag{2.5}$$

where c_j are trivially expressed using the stoichiometric coefficient of the reactions. For the present C-atom following paths, the coefficients c_j are all equal to 1. In previous work,[8−11] we have formulated the probabilities $P_j(t_0, t_f)$ for general kinetics mechanisms

$$P_{path} = \frac{1}{N}\sum_{q=1}^{N} P_n(t_n^q, t_f)\prod_{k=1}^{n}(\Gamma_k - 1(t_k^q)(1 - P_{min}^{k-1}(t_k^q))) \tag{2.6}$$

where P_n is the survival probability of species n from time t_n to t_f and Γ_{k-1} is the branching ratio for reaction $k - 1$ on the pathway. Equation 2.6 represents a Monte Carlo integration of an n-dimensional time-order expression where N is chosen to be large enough for convergence. Using these expressions, it is possible to deconstruct any observable in terms of the underlying chemical pathways. For example, the relative production of CH_2O(g) and CO(g) can be traced to separate pathways leading to those species from the MeOH precursor.

Also, the turnover frequency can usually be computed directly using eq 2.5. Thus, if the production rate of CO(g) is desired, then rate = k_{desorp}[CO(ad)] where [CO(ad)] is given by eq 2.5.

III. ENUMERATION OF CHEMICAL PATHWAYS: THE FORWARD-ONLY MODEL

Chemical pathways are identified by following the carbon atom as it migrates through the chemical network. The pathways are initiated with CH_3OH adsorption and terminated with desorption of either CO or CH_2O. Obviously, we can see from Figure 1 that an infinite number of potential pathways will develop if both forward and reverse reaction steps are included. Since kinetic observables depend on probabilistic weights of the paths, however, it is most important to identify the dominant paths which can be used to converge the expansion (eq 2.5). For most conditions we find that "forward-only" pathways, in which the reverse reactions are ignored, are by far the most important. This is due in large part to the very low H-atom concentrations on the surface since H_2 readily desorbs. These paths are distinguished by the order in which

DOI: 10.1021/acs.jpcc.8b09415
J. Phys. Chem. C 2018, 122, 28158−28172

the H-atoms are abstracted from the evolving moiety and whether the product desorbs as either CH_2O or CO. It is easily seen that there are only six possible forward-only paths in this model:

$$CH_3OH \xrightarrow[R1]{} CH_3O \xrightarrow[R2]{} CH_2O \xrightarrow[R3]{} HCO \xrightarrow[R4]{} CO \xrightarrow[D_{CO}]{} CO(g) \quad (P1)$$

$$CH_3OH \xrightarrow[R5]{} CH_2OH \xrightarrow[R6]{} HCOH \xrightarrow[R7]{} COH \xrightarrow[R8]{} CO \xrightarrow[D_{CO}]{} CO(g) \quad (P2)$$

$$CH_3OH \xrightarrow[R5]{} CH_2OH \xrightarrow[R9]{} CH_2O \xrightarrow[R3]{} HCO \xrightarrow[R4]{} CO \xrightarrow[D_{CO}]{} CO(g) \quad (P3)$$

$$CH_3OH \xrightarrow[R5]{} CH_2OH \xrightarrow[R6]{} HCOH \xrightarrow[R10]{} HCO \xrightarrow[R4]{} CO \xrightarrow[D_{CO}]{} CO(g) \quad (P4)$$

$$CH_3OH \xrightarrow[R1]{} CH_3O \xrightarrow[R2]{} CH_2O \xrightarrow[D_{CH2O}]{} CH_2O(g) \quad (P5)$$

$$CH_3OH \xrightarrow[R5]{} CH_2OH \xrightarrow[R9]{} CH_2O \xrightarrow[D_{CH2O}]{} CH_2O(g) \quad (P6)$$

We have dropped the abstracted H-atoms from these equations for brevity. In this reduced scheme, paths 1−4 yield the CO(g) product while paths 5−6 yield $CH_2O(g)$. In Figure 2 we graphically represent these forward pathways. We find

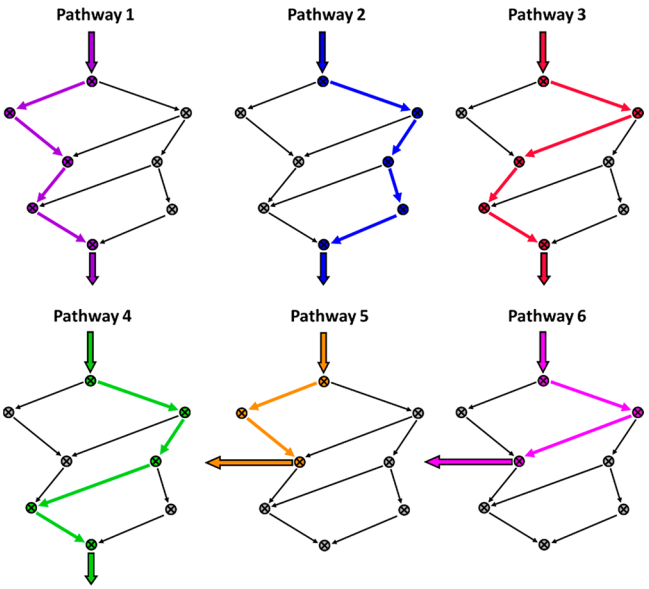

Figure 2. Six forward chemical pathways that deliver a C-atom to the CO(g) product (pathways 1−4) or the $CH_2O(g)$ product (pathways 5−6).

that this forward-only model provides a very accurate representation for the MeOH decomposition process except for high surface coverages on select metals. As a typical representative example, in Figure 3 we show the surface concentration of various intermediates versus time for a kinetic simulation on Pd(111) in which the surface is initially clean. For the time-dependent relaxation to steady state, conventional kinetic simulation is seen to give nearly identical results as the forward-only SOHR model. When necessary, however, we shall include additional pathways that include backward (recombination) reaction steps to converge the SOHR expansion.

It is seen that the choice of which forward pathway is followed by a C-atom is set at four key branching points in the reaction network.

$$CH_3OH \xrightarrow[R1\ (R5)]{} CH_3O\ (CH_2OH) \quad (a)$$

$$CH_2OH \xrightarrow[R9\ (R6)]{} CH_2O\ (CHOH) \quad (b)$$

$$CH_2O \xrightarrow[D_{CH2O}\ (R3)]{} CH_2O(g)\ (CHO) \quad (c)$$

$$CHOH \xrightarrow[R10\ (R7)]{} CHO\ (COH) \quad (d)$$

At the first branching juncture (eq a), a weakly adsorbed MeOH molecule can react to form either CH_3O through R1, $CH_3OH \xrightarrow[R1]{} CH_3O + H$, or CH_2OH through reaction R5, $CH_3OH \xrightarrow[R5]{} CH_2OH + H$. Pathways P2, P3, P4, and P6 follow the R5 reaction to CH_2OH while pathways P1 and P5 follow the R1 branch to CH_3O. Via eq b, the CH_2OH can dissociate either by reaction R9, $CH_2OH \xrightarrow[R9]{} CH_2O + H$, or by reaction R6 to $CH_2OH \xrightarrow[R6]{} HCOH + H$. Hence, pathways P3 and P6 follow reaction R9 while pathways P2 and P4 follow reaction R6. Once CH_2O is formed on the surface, via eq c it can either dehydrogenate via reaction R3, $CH_2O \xrightarrow[R3]{} HCO + H$ or desorb, intact, into the gas phase via D_{CH2O}. Thus, paths P1 from P3 follow reaction R3 while paths P5 and P6 follow the desorption D_{CH2O}. The final branching point (eq d) is for the CHOH species that can react via R10, $HCOH \xrightarrow[R10]{} HCO + H$ or R7, $HCOH \xrightarrow[R7]{} COH + H$. Pathway P4 follows the R10 branch while pathway P2 follows R7.

For the forward-only model at low surface coverage, it is possible to approximate the steady state pathway probabilities of eq 2.4 using very simple expressions. If the rate coefficients for the forward dissociation reactions are given by $k_i(T)$, then the reaction branching ratios at junctures in eqs a−d are given by

$$\Gamma_{a,1} = \frac{k_1}{k_1 + k_5} \quad \Gamma_{a,5} = \frac{k_5}{k_1 + k_5} \quad (3.1)$$

$$\Gamma_{b,6} = \frac{k_6}{k_6 + k_9} \quad \Gamma_{b,9} = \frac{k_9}{k_6 + k_9} \quad (3.2)$$

$$\Gamma_{c,3} = \frac{k_3}{k_3 + D_{CH2O}} \quad \Gamma_{c,D} = \frac{D_{CH2O}}{k_3 + D_{CH2O}} \quad (3.3)$$

$$\Gamma_{d,7} = \frac{k_7}{k_7 + k_{10}} \quad \Gamma_{d,10} = \frac{k_{10}}{k_7 + k_{10}} \quad (3.4)$$

Under steady state conditions at low coverage, eq 2.4 can be well-approximated by the appropriate product of these branching ratios along the pathways, i.e.

$$\text{Prob(P1)} \approx \Gamma_{a,1}\cdot\Gamma_{c,3} \quad (3.5)$$

$$\text{Prob(P2)} \approx \Gamma_{a,5}\cdot\Gamma_{b,6}\cdot\Gamma_{d,7} \quad (3.6)$$

$$\text{Prob(P3)} \approx \Gamma_{a,5}\cdot\Gamma_{b,9}\cdot\Gamma_{c,3} \quad (3.7)$$

$$\text{Prob(P4)} \approx \Gamma_{a,5}\cdot\Gamma_{b,9}\cdot\Gamma_{c,3} \quad (3.8)$$

DOI: 10.1021/acs.jpcc.8b09415
J. Phys. Chem. C 2018, 122, 28158−28172

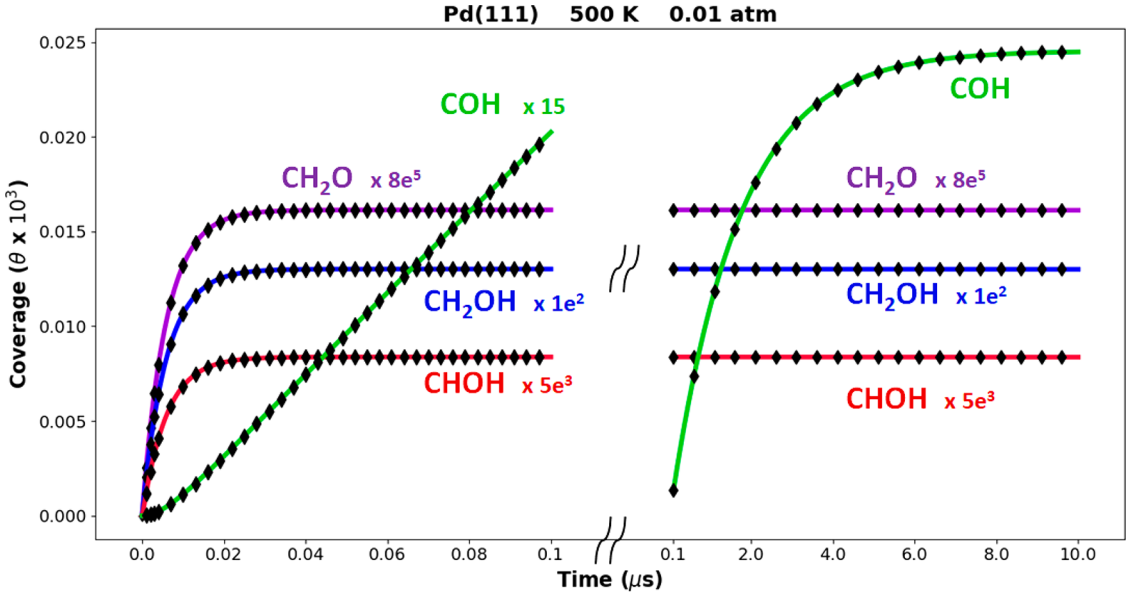

Figure 3. Surface concentrations versus time for methanol decomposition on Pd(111) computed from exact kinetic simulation and using the SOHR model employing eq 2.5. The simulations were conducted for T = 500 K and P_{MeOH} = 0.01 atm where the surface was initially uncovered and the system approaches steady state.

$$\mathrm{Prob}(P_5) \approx \Gamma_{a,1}\cdot\Gamma_{c,D} \tag{3.9}$$

$$\mathrm{Prob}(P_6) \approx \Gamma_{a,5}\cdot\Gamma_{b,9}\cdot\Gamma_{c,D} \tag{3.10}$$

These formulas work surprising well at low coverage and can be extended to higher coverage by replacing k_i in eqs 3.1−3.4 with effective values including site blocking.

IV. RESULTS AND DISCUSSION

IV.A. Energy Landscapes. The zero-point corrected energetic landscapes for methanol decomposition along pathways 1−6 are shown in Figure 4 for each metallic surface. It is clear that the different catalytic surfaces lead to quite distinct energetics which will be reflected in the kinetics. Of course, energetics is not the only issue since entropy and surface coverage can strongly modify the progress of the reaction. However, for modest coverage the simple forward model is accurate and easy to decipher through the energetics. An issue that is particularly important in comparing the catalytic properties of different surfaces is the branching ratio at the key branching junctures of the reaction network. While the full rate coefficient includes both energetic and entropic contributions, the zero-point corrected landscapes provide considerable insight into the kinetic behavior.

The different metal substrates are seen to have quite different barrier heights, and hence they will possess different branching probabilities at the juncture points a−d. Reaction R1 is seen to have the higher barrier for Pd, Pt, and Au while reaction R5 has a higher barrier for Cu and Ag. The barriers for R1 and R5 are approximately equal for the Ni, Rh, and Ir surfaces. The lower barrier for R5 on Cu and Ag is consistent with the previous reports[63,82] and is due to the stronger binding energies of CH_3O compared to CH_2OH on these surfaces. At juncture b for the CH_2OH species, we see that energetics favor reaction R6 over R9 for Rh, Pt, and Ni, while for Au and Ag the barriers are lower for R9. Roughly equal zero-point corrected barriers for Ir, Cu, and Pd suggest that these metals may exhibit appreciable kinetic branching at this step. For CHOH branching, juncture c, the metals Rh, Ir, Cu, Pd, and Ni have lower barriers for R7 favoring COH production while the opposite is true for Au, Pt, and Au. Finally, we see that, at the final juncture, eq d, the desorption energy for $CH_2O \xrightarrow[D_{CH2O}]{} CH_2O(g)$ is lower than the reaction barrier for $CH_2O \xrightarrow[R_3]{} CHO + H$ for the metals Au and Ag, while the other metals seem to favor the reaction. However, Cu and Pt do exhibit fairly low CH_2O desorption energies. The (R3, D_{CH_2O}) juncture is an important bifurcation point distinguishing CO producing pathways, pathways P1 and P3, from CH_2O producing routes, pathways P5 and P6. Here, the Cu, Au, and Ag surfaces energetically favor desorption while the remaining surfaces favor reaction.

IV.B. Forward-Only Model at Low Coverage: Single Pathway Cases. At low coverages the forward-only model applies, and we can quantitatively understand much of the catalytic kinetics in terms of the 6 elementary reaction routes shown in Figure 2. As an example, in Figure 5 we show the forward pathway probabilities for each surface obtained using the exact probabilities, eq 2.6, for the case of T = 800 K and low pressure P_{MeOH} = 0.01 atm. Under these low coverage conditions, eqs 3.5−3.10 are accurate to within a few percent. The mechanistic behavior of four of the surfaces is seen to be quite simple, namely, for Ag, Au, Cu, and Pt, which are each dominated by a single chemical pathway. The Ag, Au, and Cu surfaces produce nearly 100% CH_2O product through either pathway P5 or P6 while Pt yields CO product through path P1. This result is easily understood from the branching ratios at the juncture points, which in turn largely reflect the energetics shown in Figure 4. For Ag and Cu, the lower barrier for CH_3O formation strongly selects its formation over that of CH_2OH, i.e., $\Gamma_{a,1} \approx 1$, while the low desorption energy, Ag (0.03 eV) and Cu (0.18 eV), makes $CH_2O(g)$ formation much more rapid than reaction to CHO*, $\Gamma_{c,D} \approx 1$. Hence, we find $\mathrm{Prob}(P_5) \approx \Gamma_{a,1}\cdot\Gamma_{c,D} \approx 1$. For Au, on the other hand, the barriers strongly favor CH_2OH formation over CH_3O at

DOI: 10.1021/acs.jpcc.8b09415
J. Phys. Chem. C 2018, 122, 28158−28172

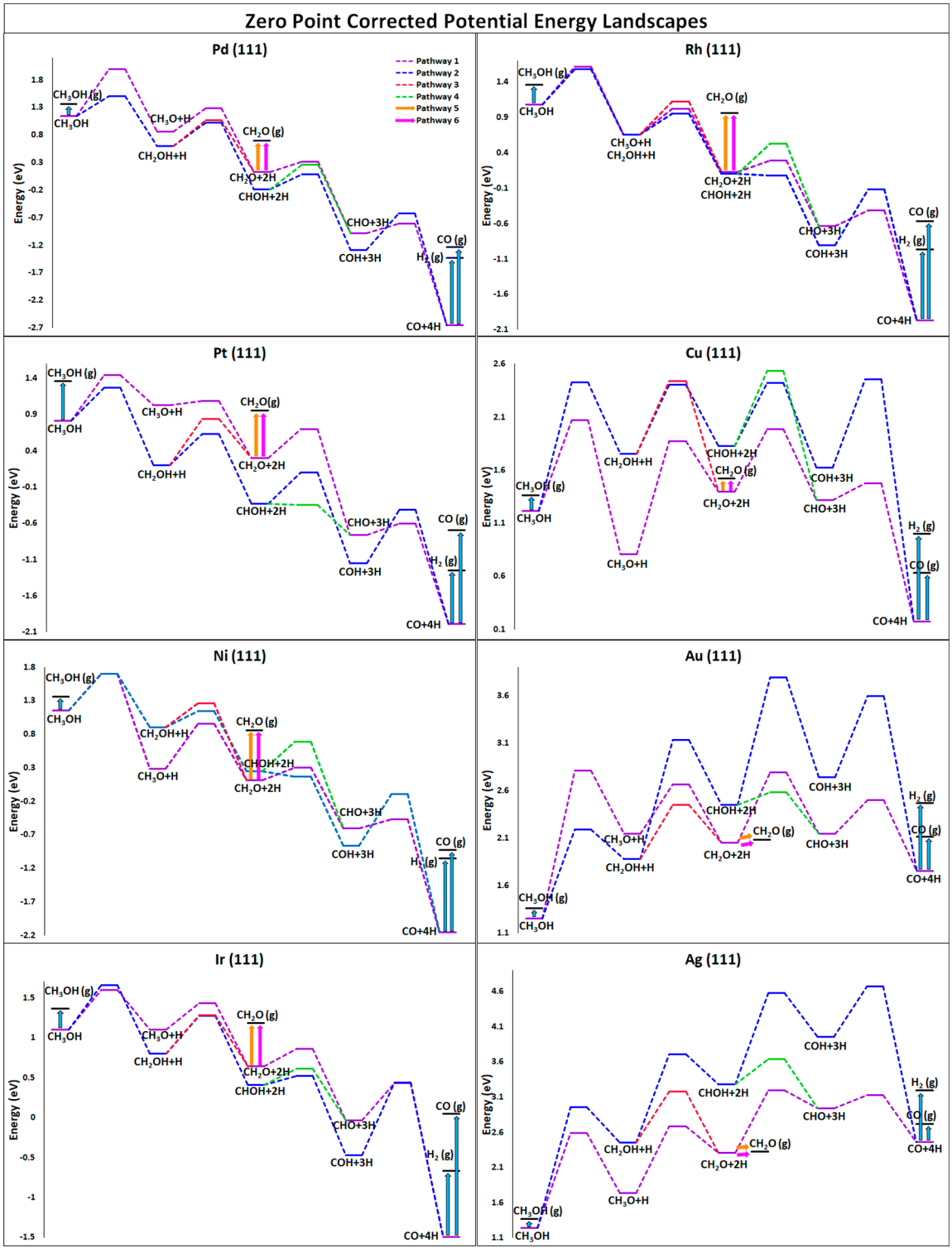

Figure 4. Zero-point corrected energetic landscapes along the six forward pathways shown in Figure 2.

juncture a, and CH_2O^* over CHOH* at juncture b, and $CH_2O(g)$ over CHO at juncture c. Hence, we have $\mathrm{Prob}(P_6) \approx \Gamma_{a,5}\cdot\Gamma_{b,9}\cdot\Gamma_{c,D} \approx 1$. Similar reasoning for the Pt surface implies $\mathrm{Prob}(P_1) \approx \Gamma_{a,1}\cdot\Gamma_{c,3} \approx 1$.

From a mechanistic point of view, the methanol decomposition chemistry on the four surfaces Pd, Rh, Ni, and Ir are the more complex and, therefore, the more interesting cases. It is seen that the decomposition occurs through several simultaneous mechanisms for these surfaces. We shall investigate two cases in detail, Pd and Ir which are found to exhibit more complicated kinetic behavior as functions of temperature and pressure.

IV.C. Pd(111). Even under conditions of low surface coverage, it is seen in Figure 5 that methanol decomposition on Pd(111) is found to occur with appreciable probability along four kinetic pathways at T = 800 K. This reflects several close lying barrier energies at juncture points, or, more accurately, the approximate equality of free energies of

DOI: 10.1021/acs.jpcc.8b09415
J. Phys. Chem. C 2018, 122, 28158−28172

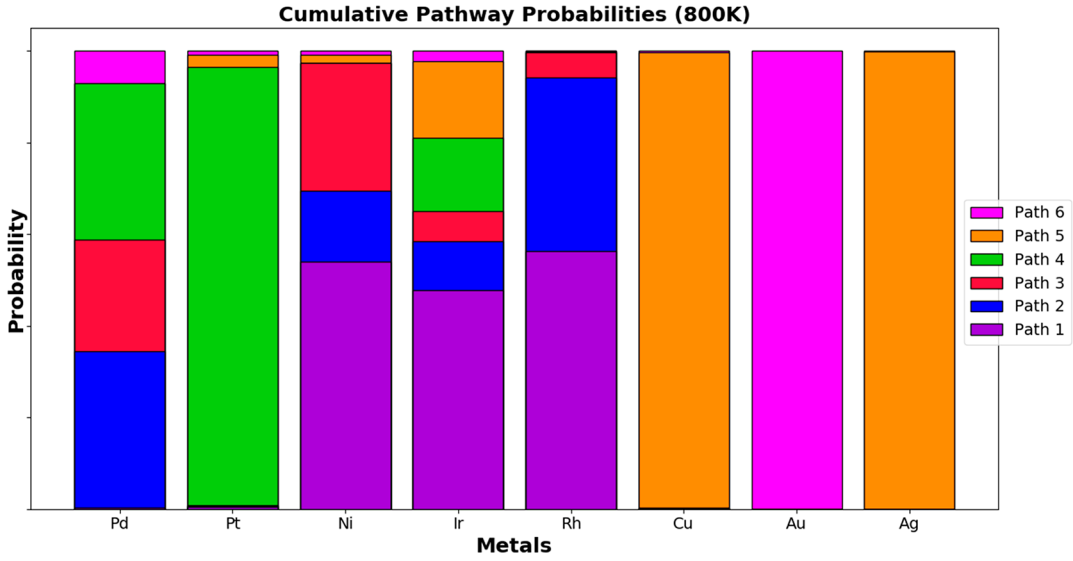

Figure 5. Pathway probabilities at steady state for eight surfaces computed for conditions of T = 800 K and P_{MeOH} = 0.01 atm. The total surface coverage under these conditions is low.

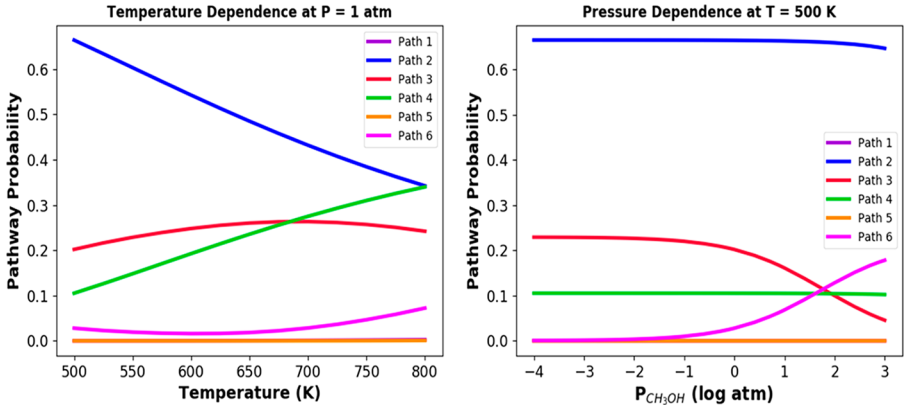

Figure 6. Temperature (left) and pressure (right) dependence of methanol decomposition pathway probabilities for pathways P1−P6 on Pd(111). The probability for path P1 is negligible under these conditions.

activation that determine the values of the rate coefficients. To further explore the kinetic behavior of MeOH on Pd(111), we have computed the temperature and pressure dependence of all the important pathway probabilities. It was found that backtracking pathways involving recombination reactions do not play an important role and pathways P1−P6 provide an excellent representation of the full kinetics. As seen in the left panel of Figure 6, there is a clear temperature dependence of the pathway probabilities at low pressures and hence low coverage. At low temperatures near 500 K, path P2 is clearly dominant. However, it decreases in importance as temperature increases to 800 K largely due to the growth of the probability of path P4. Pathway P3 is important as well and is roughly constant in probability versus T although it exhibits a modest maximum at the middle temperatures, ∼600 K. There is a small but nonzero probability for the production of CH_2O(g) product through pathway P5 that becomes slightly larger at higher temperatures. The high desorption energy of CH_2O* constrains this to be a minor channel at low pressures. Only very tiny contributions from paths P1 and P6 arise since the barrier for R1 is prohibitively large.

The temperature dependence of the MeOH decomposition chemistry on Pd(111) at low P is fairly easy to explain using the forward-only model. The main effect is the growth of the P4 channel at the expense of the P2 channel as T increases. At 800 K the probabilities for P2 and P4 become approximately equal. From Figure 2 we see that pathway P2 splits from P4 at juncture d, i.e., $\mathrm{CHOH} \xrightarrow[\mathrm{R10\ (R7)}]{} \mathrm{CHO\ (COH)}$. The low-pressure branching fractions $\Gamma_{d,7}$ and $\Gamma_{d,10}$ depend on the rate coefficients k_7 and k_{10} through eq 3.4 where, trivially, $\Gamma_{d,7} + \Gamma_{d,10} = 1$. The lower zero-point corrected barrier ΔE_0 for R7 (0.27 eV) compared to R10 (0.45 eV) modestly enhances P2 over P4 at low T. However, the larger entropy of activation in the pre-exponential factors in k_{10} compared to k_7 (due to looser TS frequencies) enhances P4 at high temperature. Hence, the rate coefficient k_7 and k_{10} actually become nearly equal at T = 800 K leading to the near equality of Prob(P2) and Prob(P4). The pathway P3 splits from P2 and P4 at juncture b, i.e., $\mathrm{CH_2OH} \xrightarrow[\mathrm{R_9\ (R_6)}]{} \mathrm{CH_2O\ (CHOH)}$. It is seen that ΔE_0 values for R9 (0.47 eV) and R6 (0.42 eV) are roughly equal as are the free energies of activation, implying little temperature dependence of $\Gamma_{b,6}$ and $\Gamma_{d,7}$. As a result we expect, and in fact we see, that Prob(P3)/(Prob(P2) + Prob(P4)) ≈ constant.

DOI: 10.1021/acs.jpcc.8b09415
J. Phys. Chem. C 2018, 122, 28158−28172

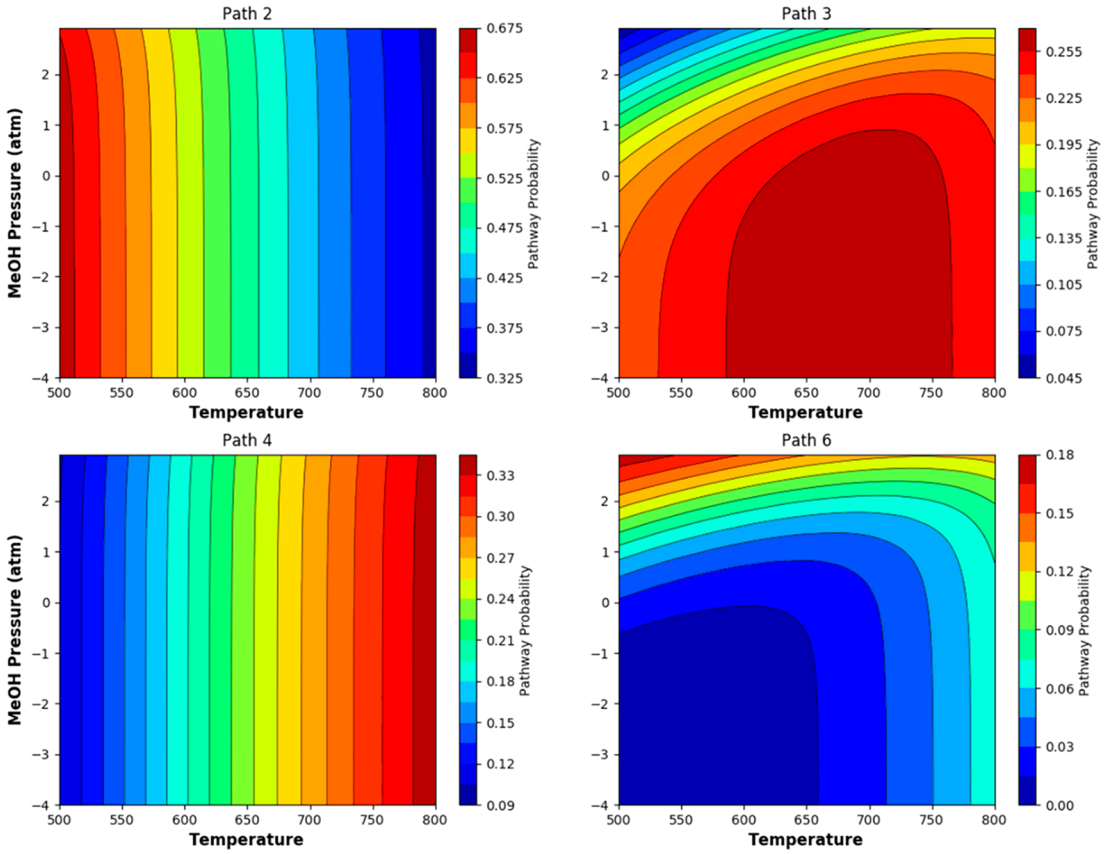

Figure 7. Pathway probabilities as a function of (T, P) for P2, P3, P4, and P6 for MeOH decomposition on Pd(111).

The chemistry of methanol decomposition on Pd(111) deviates from the simplest forward-only model at higher pressures when the surface coverage grows larger. This is potentially due to two physical effects arising from the site blocking included in the full microkinetic model: (1) the change in the relative values of the reaction rates due to the second order nature of the rate laws, i.e., (for RH + * → H + R)$k{\cdot}\theta_{RH}\theta$*, and (2) the proliferation of new reaction pathways due to reverse reactions, i.e., H + R → RH + *. These effects can have a large influence on the observed catalytic properties of the system. As we have noted already, the reverse reactions are not important for Pd(111), and the pressure effects are found to result from changes in the reaction rates.

In the right panel of Figure 6 the pathway probabilities for pathways P1−P6 are shown versus pressure at fixed temperature, T = 500 K. There is clearly a large effect that results in the P5 pathway for $CH_2O(g)$ growing into a major channel above $P_{MeOH} \approx 50$ atm. It is seen that the strongest pressure-dependent effect at T = 500 K is the nearly inverse growth of P5 at the expense of P3, while the other pathway probabilities show little change. From Figure 2 we note that path P5 splits from P3 at juncture c: $CH_2O \xrightarrow[D_{CH2O}\ (R_3)]{} CH_2O(g)(CHO + H)$. The associated branching fractions $\Gamma_{c,3}$ and $\Gamma_{c,D}$ are special in that they are expected to strongly depend on surface converge. Specifically, since in our model the surface reaction $CH_2O + * \xrightarrow[R3]{} CHO + H$ requires a free site while the desorption process $CH_2O \xrightarrow[D_{CH2O}]{} CH_2O(g)$ does not, the desorption should be enhanced at high coverage. In fact, the results in Figure 6 seem to follow this pattern *vis a vis* paths P5 and P3. The remaining branching fractions for the forward-only model are independent of coverage since all surface reactions R1−R10 equally require one free site to take place.

While Figure 6 shows the probabilities when T and P are varied separately, it is interesting to consider a wider range of reactor conditions and, thus, we have found pathway probabilities in a full two-dimensional representation. The pathway probabilities were computed on a two-dimensional grid in the (T, P) plane in the range 500−800 K and 10^{-4} to 1000 atm for steady state conditions. By direct computation using eq 2.6, it was found that the forward-only pathways were by far the most important, with reverse reactions playing only a minor role for all conditions studied. The contour diagrams for probabilities for P2, P3, P4, and P6 are shown in Figure 7. It is seen that the probabilities for P2 and P4 are largely independent of pressure over the full parameter range while significant (T, P) correlations develop for P3 and P6. As suggested by the previous discussion concerning Figure 6, the pressure dependence of the sum Prob(P3) + Prob(P6) is largely suppressed. We find the surface is almost completely covered at low temperatures, T < 600 K, and high pressures, P > 10 atm (see Supporting Information). However, at the higher temperatures, i.e., T > 700 K, a significant number of free sites continue to exist even up to 1000 atm. The dominant surface species is always found to be CO* although significant levels of H-atom coverage also occur at high pressure.

The most interesting variation observed in the pathway probabilities related to the product selectivity, i.e., the probabilities of pathways leading to CO(g) relative to those leading to $CH_2O(g)$ formation. This quantity is important as it

DOI: 10.1021/acs.jpcc.8b09415
J. Phys. Chem. C 2018, 122, 28158−28172

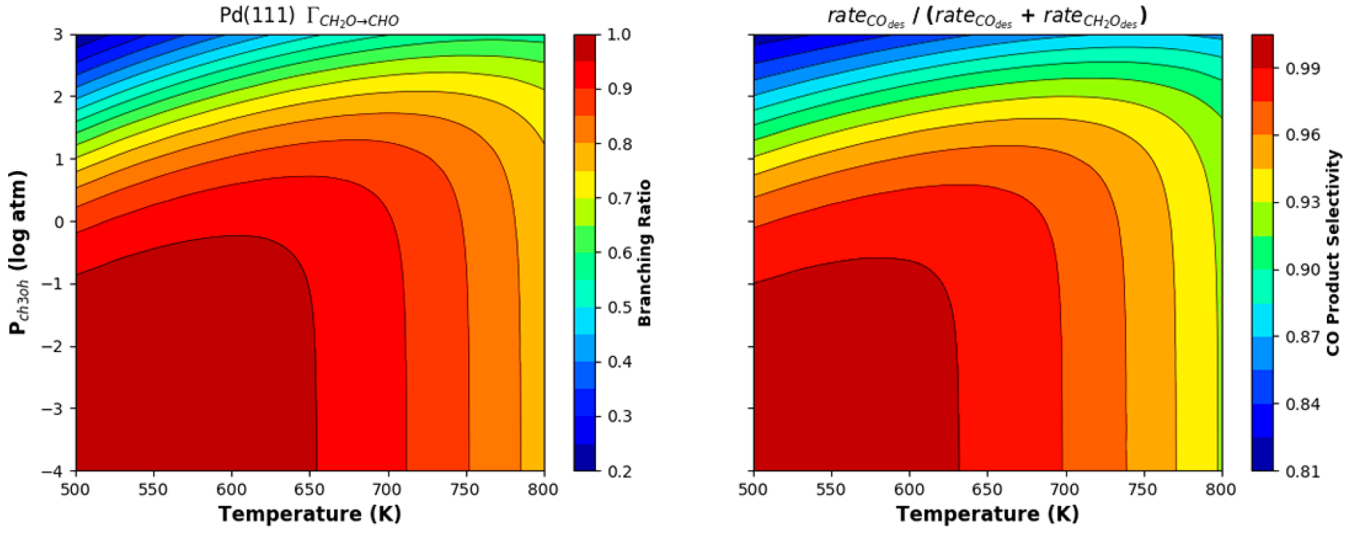

Figure 8. Product selectivity for methanol decomposition on Pd(111) as a function of temperature and pressure. The right panel shows the selectivity product production rates at steady state. In the left panel the branching fraction $\Gamma_{c,3}$, which is probability of following the reaction R3 at juncture c, i.e., $CH_2O \xrightarrow[R_3]{} CHO$.

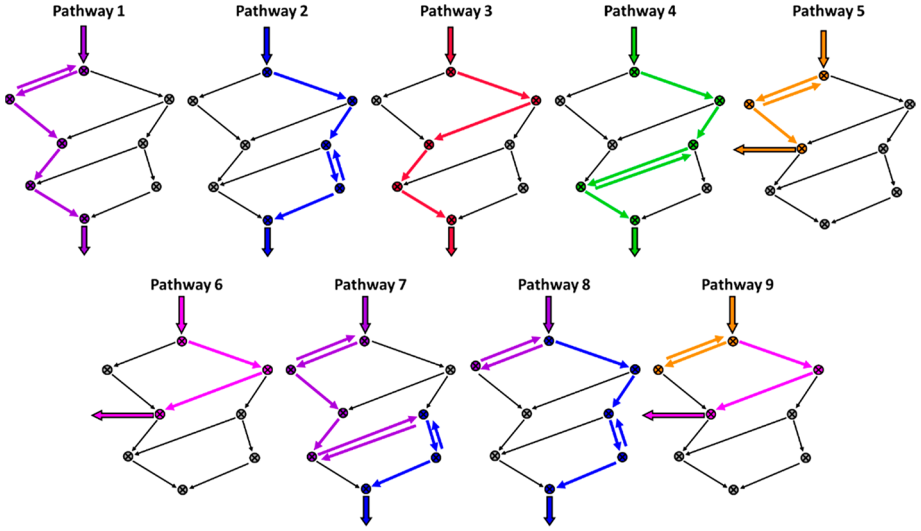

Figure 9. Most important chemical pathways for MeOH decomposition on Ir(111). The reversible arrows indicate steps with a high degree of backtracking and chemical chattering. Pathways 7−9 switch reaction routes.

is potentially a sensitive experimental observable. The product branching ratio is obtained directly from the pathway probabilities via

$$F_{CH_2O}(T, P) = \frac{P_5 + P_6}{\sum_{i=1}^{6} P_i} \quad F_{CO}(T, P) = \frac{P_1 + P_2 + P_3 + P_4}{\sum_{i=1}^{6} P_i} \tag{4.1}$$

In the right panel of Figure 8 we show the product branching computed from production rates in the (T, P) plane. It is seen that, at low pressures, CO(g) is the dominant product with the chemistry proceeding mostly through pathways P2, P3, and P5. At higher pressure, pathway P5 becomes increasingly important and, hence, the CH_2O(g) production rate grows larger. The production of CH_2O(g) can become as high as 20% in the high-P and low-T parameter region. As the previous discussion implies, almost all the effect traces back to juncture c where the key branching ratios $\Gamma_{c,3}$ and $\Gamma_{c,D}$ are strongly coverage-dependent. This is emphasized in the left panel of Figure 8 by plotting the quantity $\Gamma_{c,3}$ in the (T, P) plane, similar to the product selectivity. Clearly, the behavior of the branching fraction $\Gamma_{c,3}$ quantitatively reproduces the product selectivity which is a great simplification of the surface kinetics.

IV.D. Ir(111). The decomposition kinetics on the Ir(111) substrate is the most complex case of the eight catalytic surfaces considered. At low pressures, all six forward pathways show non-negligible probabilities since there exists significant branching at the four juncture points. Furthermore, at high pressures the forward-only model shows appreciable breakdown, and additional backtracking chemical pathways grow in importance. A key distinction between the Ir(111) surface and the other metals is the relatively low activation barriers observed for a number of the recombination reactions which therefore greatly enhances the probability of backtracking pathways.

We can distinguish between two types of additional reaction pathways we have identified using the SOHR method. (1) Chattering pathways, where a H-atom dissociates from the

DOI: 10.1021/acs.jpcc.8b09415
J. Phys. Chem. C 2018, 122, 28158−28172

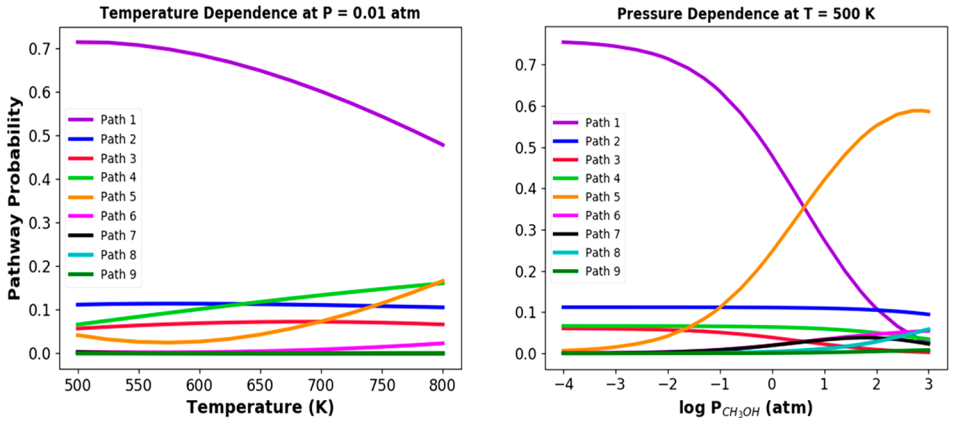

Figure 10. T and P dependence of the pathway probabilities for P1−P9 (shown in Figure 9) on Ir(111). The left panel shows the T dependence holding P fixed at 0.01 atm, while the right panel shows the P dependence holding T fixed at 500 K.

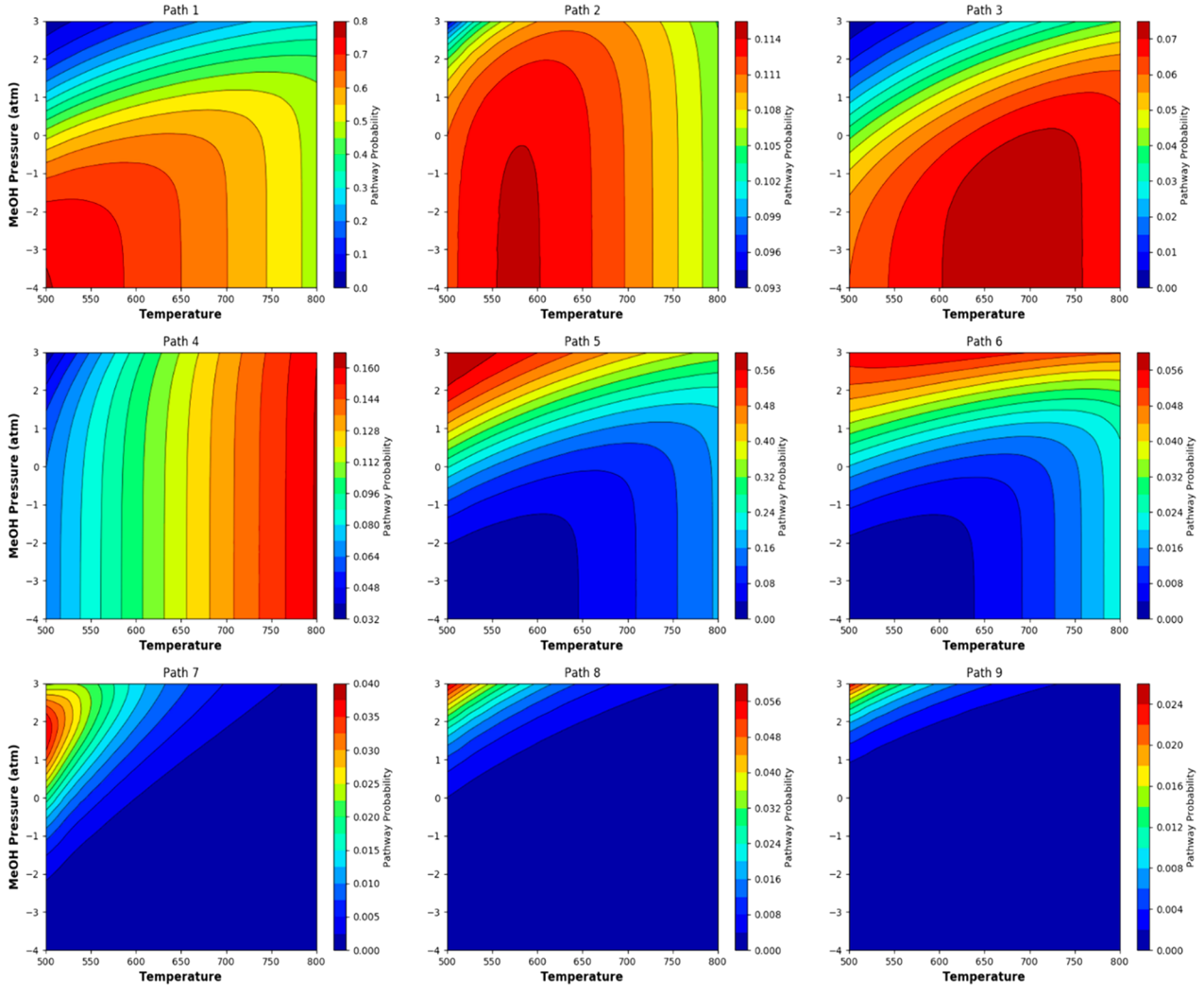

Figure 11. Pathway probabilities for pathways P1−P9 (defined in Figure 9) for Ir(111) as a function of (T, P).

moiety but then recombines with it one or more times, i.e., RH + * → R + H → RH + * → R + H → ... (2) Pathway switching routes in which the recombination/dissociation process results in an alteration of the chemical identity of the moiety, i.e., RH + * → R + H → RH → R′ + H... We computed all the important pathway probabilities using eq 2.6, which can be applied to pathways of any length and complexity. Since the phenomenon of chemical chattering, RH + * ↔ R + H, does not ultimately change the reaction route (P1−P6) followed by the carbon containing moiety, we have combined the chattering pathways with the nominal forward pathway which are labeled P1−P6. The probabilities of these reaction routes of course need to be summed over paths with 0, 1, 2, ... chattering events RH + * ↔ R + H that occur at various steps.

DOI: 10.1021/acs.jpcc.8b09415
J. Phys. Chem. C 2018, 122, 28158−28172

The pathway switching routes, on the other hand, are entirely new. In Figure 9 we show the highest probability pathways that occur for the Ir(111) substrate. In the P1−P6 pathways, we indicate the steps at which chattering is most important with reversible arrows. The pathways P7−P9 are the most important pathway switching routes. These pathways are found to contribute ∼10% of the reaction flux under the most favorable conditions.

The probabilities for P1−P9 were computed as separate functions of T and P in Figure 10. In the left panel, the T dependence of the probabilities is shown at fixed pressure P = 0.01 atm. Since surface coverage is low at this pressure, the reverse reaction rates are very small and, hence, the probabilities for P7−P9 are negligible. However, the probabilities for P1−P6 are all appreciable with P1 being the largest. The value of Prob(P1) falls from 70% at T = 500 K to less than 50% of the total at T = 800 K. The temperature variation of the low pressure results is completely consistent with the forward-only probabilities given by eqs 3.5−3.10. The barriers for several of the reactions are roughly commensurate leading to significant branching of the reactive flux as it moves through the reaction network leading to the wide distribution of probabilities observed in Figure 10.

The variation of the Ir(111) pathway probabilities versus pressure holding T fixed at 500 K is shown in the right-hand panel of Figure 10. Clearly, the most dramatic effect is the falloff of Prob(P1) from 0.7 to nearly 0 by P = 1000 atm. Likewise, the probability for P3 falls from 0.1 to 0 as pressure increases. These probability losses are compensated by growth in the probabilities for pathways P5−P9. Similar to the Pd(111) case, the main explanation for this reciprocal behavior involves site blocking at juncture c $CH_2O \xrightarrow[D_{CH2O}\ (R_3)]{} CH_2O(g)\ (CHO + H)$. At the high surface coverage accompanying high pressure, the loss of free sites strongly shifts the branching ratio away from favoring CHO production (due to a lower barrier) to favoring desorption of $CH_2O(g)$. This inhibits both the P1 and P3 pathways, and thus, much of the reaction flux shifts to pathway P5 at high coverage. However, due to the recombination reactions $CH_2O + H \rightarrow CH_2OH$ (BR5) and $CHO + H \rightarrow CHOH$ (BR10), backtracking pathways also begin to grow in importance. The net result is that, at high pressures, kinetic observables such as the turnover frequency can no longer be ascribed to a single rate limiting process.

We have computed the pathway probabilities and the other steady state kinetic properties for Ir(111) in a two-dimensional representation (T, P) over the range T = 500−800 K and P = 10^{-4} to 1000 atm in a manner similar to that used for Pd(111). In Figure 11 we show the pathway probabilities for P1−P9 as contour plots. The coverages were also determined as a function of (T, P), and it was found that the main surface species is CO, but significant levels of H and COH also develop at high pressures. It is seen in Figure 11 that the probabilities for P1 and P5 show an anticorrelated behavior similar to that evinced by P3 and P5 for reaction on the Pd(111) surface. That is, as pressure increases, the P1 declines in probability while P5 grows. However, unlike the Pd(111) case, the probability loss from P1 is distributed over several other pathways due to the recombination reactions. The pathways P7−P9 exhibit appreciable probabilities only when the surface coverages grow large, since the reverse reactions require H-atoms to proceed. Two of the smaller probability paths, P3 and P4, show maxima at intermediate temperatures.

It is interesting to consider the predictions of the microkinetic model for the final product selectivity on the Ir(111) surface. The ratio of production rates into the CO(g) and $CH_2O(g)$ products can be directly computed from the kinetic simulations. It is found that those results almost exactly match the predictions of the SOHR method where the CO(g) production occurs through pathways P1−P4, P7, and P8 while $CH_2O(g)$ production occurs through pathways P5, P6, and P9. The selectivity of products is depicted in Figure 12 as a function of (T,P). For low MeOH pressures, i.e. P < 1 atm, the CO(g) product dominates. However, at higher pressure the $CH_2O(g)$ channel becomes increasingly important and can account for up to 85% of the product yield. Clearly, this sensitive experimental observable can be used to assess the accuracy of the microkinetic model. The SOHR analysis pinpoints the key to product selectivity to be juncture c and the branching ratios for reactions $CH_2O \xrightarrow[D_{CH2O}\ (R_3)]{} CH_2O(g)(CHO + H)$.

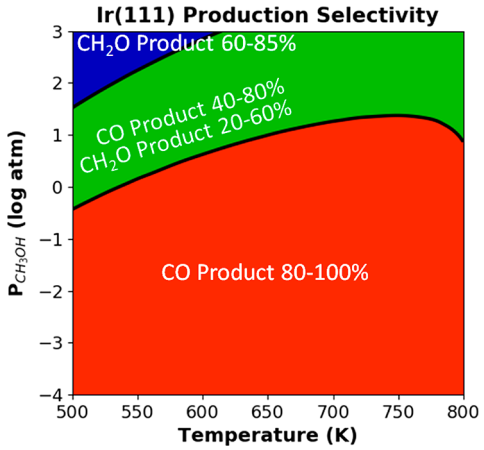

Figure 12. Product selectivity for MeOH decomposition on Ir(111) as a function of (T, P).

V. CONCLUSIONS

The kinetics of surface catalyzed decomposition of methanol to $CO + 2H_2$ or $CH_2O + H_2$ on eight metallic surfaces were studied theoretically using a microkinetic model that included 10 reversible surface reactions and adsorption/desorption processes. Coverage dependence was modeled using a site-blocking scheme for the mass action kinetics. Using data obtained from high-level DFT calculations, temperature-dependent rate coefficients were computed using TST. The rate coefficients were fit to generalized Arrhenius expressions and are presented in the Supporting Information. Using the sum over histories representation (SOHR), the chemical pathways leading to products were identified and the associated probabilities were computed over broad ranges of temperature and pressure. Under conditions of low to moderate MeOH pressures, it was found that the decomposition kinetics could be accurately modeling using six "forward" pathways which do not include any reverse (recombination) reactions. These paths involve the sequential abstraction of H-atoms from the C-atom containing moiety. The pathways differ from one another by the order in which

DOI: 10.1021/acs.jpcc.8b09415
J. Phys. Chem. C 2018, 122, 28158−28172

the abstraction reactions occur. Under steady state conditions at low pressures, the probabilities of these pathways could be accurately approximated as the product of branching ratios at four key juncture points in the kinetic scheme. When the MeOH pressure was increased, two important modifications to this approximation occur. First, site-blocking due to the growth of surface coverage will change the branching ratios at juncture points of the reaction network. Second, the growth of surface coverage of H-atoms will cause the reverse reactions to grow in importance which potentially modifies the reaction routes. These effects were both well-modeled using the SOHR method which explicitly decomposes the kinetics into the contributions from individual reaction pathways. It was seen that the site-blocking phenomena can lead to dramatic changes in the product selectively, i.e., the ratio of final products going to the $CO(g) + 2H_2(g)$ channel versus the $CH_2O(g) + H_2(g)$ channel. The growth of rates for reverse reactions tends to distribute the probabilities of reaction over a broader range of reactions pathways.

It was observed that the reaction route followed for MeOH decomposition was strongly affected by the choice of metal surface. The kinetics on several metal surfaces were dominated by a single reaction pathway, viz., Cu, Ag, Au, and Pt. The particular pathway followed, however, was different depending on the branching ratios at the juncture points. The remaining four surfaces exhibited more complicated kinetics following a number of competing chemical pathways. We studied the kinetics of two of these case, Pd(111) and Ir(111), in detail. It was found that reaction routes followed in these cases are strongly dependent on the temperature and pressure under which the reaction occurs. These effects could be quantitatively understood using the SOHR method. The microkinetic model itself has some limitations. We have assumed that the lateral interactions between adsorbed species are negligible and have included coverage-dependent effects only through the site-blocking mechanism. This approximation could clearly be improved using more extensive DFT modeling. We have also assumed that the diffusion barriers are small compared to the reaction barriers so that the kinetics can be modeled using a homogeneous representation. A more realistic model could clearly be constructed either a kinetic Monte Carlo representation or through a reaction-diffusion model. Such treatments may be quite useful in representing the kinetics at high pressures.

■ ASSOCIATED CONTENT

Supporting Information

The Supporting Information is available free of charge on the ACS Publications website at DOI: 10.1021/acs.jpcc.8b09415.

Geometries of intermediates, the activation energies and rate coefficients of the elementary steps, the vibrational frequencies of intermediates and transition states, and the surface coverages on Ir(111) and Pd(111) (PDF)

■ AUTHOR INFORMATION

Corresponding Authors

*E-mail: wxli70@ustc.edu.cn.

*E-mail: rex.skodje@colorado.edu.

ORCID

Wei-Xue Li: 0000-0003-1601-5189

Rex T. Skodje: 0000-0003-3389-9318

Notes

The authors declare no competing financial interest.

■ ACKNOWLEDGMENTS

R.T.S. and R.H.W. acknowledge the National Science Foundation of the United States through Grant CHE1664555 and the Chinese Academy of Science for support of this work. W.-X.L. acknowledges the National Key R&D Program of China (2017YFB0602205, 2018YFA0208603) and the Natural Science Foundation of China (91645202), and the Frontier Science Key Project of the Chinese Academy of Sciences (QYZDJ-SSW-SLH054). R.T.S. and R.H.W. appreciate the hospitality of the Dalian Institute for Chemical Physics and the State Key Laboratory for Reaction Dynamics for part of this work.

■ REFERENCES

(1) Somorjai, G. A.; Li, Y. *Introduction to Surface Chemistry and Catalysis*; John Wiley & Sons: Hoboken, NJ, 2010.

(2) Hammer, B.; Nørskov, J. K. Theoretical Surface Science and Catalysis − Calculations and Concepts. *Adv. Catal.* **2000**, *45*, 71−129.

(3) Nørskov, J. K.; Abild-Pedersen, F.; Studt, F.; Bligaard, T. Density Functional Theory in Surface Chemistry and Catalysis. *Proc. Natl. Acad. Sci. U. S. A.* **2011**, *108*, 937−943.

(4) Burke, K. Perspective on Density Functional Theory. *J. Chem. Phys.* **2012**, *136*, 150901.

(5) Reuter, K. Ab Initio Thermodynamics and First-Principles Microkinetics for Surface Catalysis. *Catal. Lett.* **2016**, *146*, 541−563.

(6) Stamatakis, M.; Vlachos, D. G. Unraveling the Complexity of Catalytic Reactions via Kinetic Monte Carlo Simulation: Current Status and Frontiers. *ACS Catal.* **2012**, *2*, 2648−2663.

(7) Liu, D. J.; Evans, J. J. Realistic multisite lattice-gas modeling and KMC simulation of catalytic surface reactions: Kinetics and multiscale spatial behavior for CO-oxidation on metal (1 0 0) surfaces. *Prog. Surf. Sci.* **2013**, *88*, 393−521.

(8) Bai, S.; Skodje, R. T. Simulating Chemical Kinetics Without Differential Equations: A Quantitative Theory Based on Chemical Pathways. *J. Phys. Chem. Lett.* **2017**, *8*, 3826−3833.

(9) Bai, S. R.; Skodje, R. T. The Sum Over Histories Representation for Chemical Kinetics: A Quantitative Theory Based on Chemical Pathways. *Int. Rev. Phys. Chem.* **2016**, *35*, 539−567.

(10) Bai, S. R.; Zhou, D. Y.; Davis, M. J.; Skodje, R. T. Sum Over Histories Representation for Chemical Kinetics. *J. Phys. Chem. Lett.* **2015**, *6*, 183−188.

(11) Bai, S. R.; Davis, M. J.; Skodje, R. T. Sum over Histories Representation for Kinetic Sensitivity Analysis: How Chemical Pathways Change When Reaction Rate Coefficients Are Varied. *J. Phys. Chem. A* **2015**, *119*, 11039−11052.

(12) Kramer, Z. C.; Gu, X. K.; Zhou, D.; Li, W. X.; Skodje, R. T. Following Molecules through Reactive Networks: Surface Catalyzed Decomposition of Methanol on Pd(111), Pt(111), and Ni(111). *J. Phys. Chem. C* **2014**, *118*, 12364−12383.

(13) Kozuch, S.; Shaik, S. How to Conceptualize Catalytic Cycles? The Energetic Span Model. *Acc. Chem. Res.* **2011**, *44*, 101−110.

(14) Gu, X. K.; Liu, B.; Greeley, J. First-Principles Study of Structure Sensitivity of Ethylene Glycol Conversion on Platinum. *ACS Catal.* **2015**, *5*, 2623−2631.

(15) Campbell, C. T. Finding the Rate-Determining Step in a Mechanism. *J. Catal.* **2001**, *204*, 520−524.

(16) Stegelmann, C.; Andreasen, A.; Campbell, C. T. Degree of Rate Control: How Much the Energies of Intermediates and Transition States Control Rates. *J. Am. Chem. Soc.* **2009**, *131*, 8077−8082.

(17) Campbell, C. T. Future Directions and Industrial Perspectives Micro- and macro-kinetics: Their relationship in heterogeneous catalysis. *Top. Catal.* **1994**, *1*, 353−366.

(18) Dumesic, J. A. Analyses of Reaction Schemes Using De Donder Relations. *J. Catal.* **1999**, *185*, 496−505.

DOI: 10.1021/acs.jpcc.8b09415
J. Phys. Chem. C 2018, 122, 28158−28172

(19) Motagamwala, A. H.; Dumesic, J. A. Analysis of Reaction Schemes Using Maximum Rates of Constituent Steps. *Proc. Natl. Acad. Sci. U. S. A.* **2016**, *113*, E2879−E2888.
(20) Dumesic, J. A. Reply to Finding the Rate-Determining Step in a Mechanism: Comparing DeDonder Relations with the "Degree of Rate Control. *J. Catal.* **2001**, *204*, 525−529.
(21) Norskov, J. K.; Bligaard, T.; Kleis, J. Rate Control and Reaction Engineering. *Science* **2009**, *324*, 1655−1656.
(22) Feynman, R. P.; Hibbs, A. R. *Quantum Mechanics and Path Integrals*; McGraw-Hill: New York, 1965.
(23) Navarro, R. M.; Pena, M. A.; Fierro, J. L. G. Hydrogen Production Reactions from Carbon Feedstocks: Fossil Fuels and Biomass. *Chem. Rev.* **2007**, *107*, 3952−3991.
(24) Wang, S. S.; Gu, X. K.; Su, H. Y.; Li, W. X. First-Principles and Microkinetic Simulation Studies of the Structure Sensitivity of Cu Catalyst for Methanol Steam Reforming. *J. Phys. Chem. C* **2018**, *122*, 10811−10819.
(25) Wang, S. S.; Su, H. Y.; Gu, X. K.; Li, W. X. Differentiating Intrinsic Reactivity of Copper, Copper−Zinc Alloy, and Copper/Zinc Oxide Interface for Methanol Steam Reforming by First-Principles Theory. *J. Phys. Chem. C* **2017**, *121*, 21553−21559.
(26) Palo, D. R.; Dagle, R. A.; Holladay, J. D. Methanol Steam Reforming for Hydrogen Production. *Chem. Rev.* **2007**, *107*, 3992−4021.
(27) Gu, X. K.; Qiao, B. T.; Huang, C. Q.; Ding, W. C.; Sun, K. J.; Zhan, E. S.; Zhang, T.; Liu, J. Y.; Li, W. X. Supported Single Pt1/Au1 Atoms for Methanol Steam Reforming. *ACS Catal.* **2014**, *4*, 3886−3890.
(28) Gu, X. K.; Li, W. X. First-Principles Study on the Origin of the Different Selectivities for Methanol Steam Reforming on Cu(111) and Pd(111). *J. Phys. Chem. C* **2010**, *114*, 21539−21547.
(29) Cubeiro, M. L.; Fierro, J. L. G. Selective Production of Hydrogen by Partial Oxidation of Methanol over ZnO-Supported Palladium Catalysts. *J. Catal.* **1998**, *179*, 150−162.
(30) Alejo, L.; Lago, R.; Pena, M. A.; Fierro, J. L. G. Partial oxidation of methanol to produce hydrogen over Cu-Zn-based catalysts. *Appl. Catal., A* **1997**, *162*, 281−297.
(31) Choksi, T.; Greeley, J. Partial Oxidation of Methanol on MoO3 (010): A DFT and Microkinetic Study. *ACS Catal.* **2016**, *6*, 7260−7277.
(32) Suntivich, J.; Xu, Z. C.; Carlton, C. E.; Kim, J.; Han, B. H.; Lee, S. W.; Bonnet, N.; Marzari, N.; Allard, L. F.; Gasteiger, H. A.; Hamad-Schifferli, K.; Shao-Horn, Y. Surface Composition Tuning of Au−Pt Bimetallic Nanoparticles for Enhanced Carbon Monoxide and Methanol Electro-oxidation. *J. Am. Chem. Soc.* **2013**, *135*, 7985−7991.
(33) Lee, S. W.; Chen, S. O.; Sheng, W. C.; Yabuuchi, N.; Kim, Y. T.; Mitani, T.; Vescovo, E.; Shao-Horn, Y. Roles of Surface Steps on Pt Nanoparticles in Electro-oxidation of Carbon Monoxide and Methanol. *J. Am. Chem. Soc.* **2009**, *131*, 15669−15677.
(34) Ferrin, P.; Mavrikakis, M. Structure Sensitivity of Methanol Electrooxidation on Transition Metals. *J. Am. Chem. Soc.* **2009**, *131*, 14381−14389.
(35) Grabow, L. C.; Mavrikakis, M. Mechanism of Methanol Synthesis on Cu through CO2 and CO Hydrogenation. *ACS Catal.* **2011**, *1*, 365−384.
(36) Behrens, M.; Studt, F.; Kasatkin, I.; Kuhl, S.; Havecker, M.; Abild-Pedersen, F.; Zander, S.; Girgsdies, F.; Kurr, P.; Kniep, B. L.; Tovar, M.; Fischer, R. W.; Norskov, J. K.; Schlogl, R. The Active Site of Methanol Synthesis over $Cu/ZnO/Al_2O_3$ Industrial Catalysts. *Science* **2012**, *336*, 893−897.
(37) Studt, F.; Sharafutdinov, I.; Abild-Pedersen, F.; Elkjaer, C. F.; Hummelshoj, J. S.; Dahl, S.; Chorkendorff, I.; Norskov, J. K. Discovery of a Ni-Ga catalyst for carbon dioxide reduction to methanol. *Nat. Chem.* **2014**, *6*, 320−324.
(38) Hung, T. C.; Liao, T. W.; Liao, Z. H.; Hsu, P. W.; Cai, P. Y.; Lee, H.; Lai, Y. L.; Hsu, Y. J.; Chen, H. Y.; Wang, J. H.; et al. Dependence on Size of Supported Rh Nanoclusters in the Decomposition of Methanol. *ACS Catal.* **2015**, *5*, 4276−4287.
(39) Hokenek, S.; Kuhn, J. N. Methanol Decomposition over Palladium Particles Supported on Silica: Role of Particle Size and Co-Feeding Carbon Dioxide on the Catalytic Properties. *ACS Catal.* **2012**, *2*, 1013−1019.
(40) Mehmood, F.; Greeley, J.; Zapol, P.; Curtiss, L. A. Comparative Density Functional Study of Methanol Decomposition on Cu4 and Co4 Clusters. *J. Phys. Chem. B* **2010**, *114*, 14458−14466.
(41) Mehmood, F.; Greeley, J.; Curtiss, L. A. Density Functional Studies of Methanol Decomposition on Subnanometer Pd Clusters. *J. Phys. Chem. C* **2009**, *113*, 21789−21796.
(42) Garcia-Muelas, R.; Li, Q.; Lopez, N. Density Functional Theory Comparison of Methanol Decomposition and Reverse Reactions on Metal Surfaces. *ACS Catal.* **2015**, *5*, 1027−1036.
(43) Mehmood, F.; Rankin, R. B.; Greeley, J.; Curtiss, L. A. Trends in methanol decomposition on transition metal alloy clusters from scaling and Brønsted−Evans−Polanyi relationships. *Phys. Chem. Chem. Phys.* **2012**, *14*, 8644−8652.
(44) Greeley, J.; Mavrikakis, M. A First-Principles Study of Methanol Decomposition on Pt(111). *J. Am. Chem. Soc.* **2002**, *124*, 7193−7201.
(45) Greeley, J.; Mavrikakis, M. Competitive Paths for Methanol Decomposition on Pt(111). *J. Am. Chem. Soc.* **2004**, *126*, 3910−3919.
(46) Desai, S. K.; Neurock, M.; Kourtakis, K. A Periodic Density Functional Theory Study of the Dehydrogenation of Methanol over Pt(111). *J. Phys. Chem. B* **2002**, *106*, 2559−2568.
(47) Jiang, R. B.; Guo, W. Y.; Li, M.; Fu, D. L.; Shan, H. H. Density Functional Investigation of Methanol Dehydrogenation on Pd(111). *J. Phys. Chem. C* **2009**, *113*, 4188−4197.
(48) Kandoi, S.; Greeley, J.; Sanchez-Castillo, M. A.; Evans, S. T.; Gokhale, A. A.; Dumesic, J. A.; Mavrikakis, M. Predicition of Experimental Methanol Decomposition Rates on Platinum from First Principles. *Top. Catal.* **2006**, *37*, 17−28.
(49) Miller, A. V.; Kaichev, V. V.; Prosvirin, I. P.; Bukhtiyarov, V. I. Mechanistic Study of Methanol Decomposition and Oxidation on Pt(111). *J. Phys. Chem. C* **2013**, *117*, 8189−8197.
(50) Kaichev, V. V.; Miller, A. V.; Prosvirin, I. P.; Bukhtiyarov, V. I. In situ XPS and MS study of methanol decomposition and oxidation on Pd(111) under millibar pressure range. *Surf. Sci.* **2012**, *606*, 420−425.
(51) Borasio, M.; Rodriguez de la Fuente, O.; Rupprechter, G.; Freund, H. J. In Situ Studies of Methanol Decomposition and Oxidation on Pd(111) by PM-IRAS and XPS Spectroscopy. *J. Phys. Chem. B* **2005**, *109*, 17791−17794.
(52) Yudanov, I. V.; Matveev, A. V.; Neyman, K. M.; Rosch, N. How the C−O Bond Breaks during Methanol Decomposition on Nanocrystallites of Palladium Catalysts. *J. Am. Chem. Soc.* **2008**, *130*, 9342−9352.
(53) Moura, A. S.; Fajin, J. L. C.; Pinto, A. S. S.; Mandado, M.; Cordeiro, M. N. D. S. Competitive Paths for Methanol Decomposition on Ruthenium: A DFT Study. *J. Phys. Chem. C* **2015**, *119*, 27382−27391.
(54) Barros, R. B.; Garcia, A. R.; Ilharco, L. M. The Decomposition Pathways of Methanol on Clean Ru(0001), Studied by Reflection−Absorption Infrared Spectroscopy (RAIRS). *J. Phys. Chem. B* **2001**, *105*, 11186−11193.
(55) Jiang, R. B.; Guo, W. Y.; Li, M.; Zhu, H. Y.; Zhao, L. M.; Lu, X. Q.; Shan, H. H. Methanol dehydrogenation on Rh(1 1 1): A density functional and microkinetic modeling study. *J. Mol. Catal. A: Chem.* **2011**, *344*, 99−110.
(56) Xu, L. J.; Mei, D. H.; Henkelman, G. Adaptive kinetic Monte Carlo simulation of methanol decomposition on Cu(100). *J. Chem. Phys.* **2009**, *131*, 244520.
(57) Zuo, Z. J.; Wang, L.; Han, P. D.; Huang, W. Insights into the reaction mechanisms of methanol decomposition, methanol oxidation and steam reforming of methanol on Cu(111): A density functional theory study. *Int. J. Hydrogen Energy* **2014**, *39*, 1664−1679.
(58) Greeley, J.; Mavrikakis, M. Methanol Decomposition on Cu(111): A DFT Study. *J. Catal.* **2002**, *208*, 291−300.

DOI: 10.1021/acs.jpcc.8b09415
J. Phys. Chem. C 2018, 122, 28158−28172

(59) Mei, D. H.; Xu, L. J.; Henkelman, G. Potential Energy Surface of Methanol Decomposition on Cu(110). *J. Phys. Chem. C* **2009**, *113*, 4522−4537.
(60) Wang, H.; He, C. Z.; Huai, L. Y.; Liu, J. Y. Decomposition and Oxidation of Methanol on Ir(111): A First-Principles Study. *J. Phys. Chem. C* **2013**, *117*, 4574−4584.
(61) Zhou, Y. H.; Lv, P. H.; Wang, G. C. DFT studies of methanol decomposition on Ni(100) surface: Compared with Ni(111) surface. *J. Mol. Catal. A: Chem.* **2006**, *258*, 203−215.
(62) Wang, G. C.; Zhou, Y. H.; Morikawa, Y.; Nakamura, J.; Cai, Z. S.; Zhao, X. Z. Kinetic Mechanism of Methanol Decomposition on Ni(111) Surface: A Theoretical Study. *J. Phys. Chem. B* **2005**, *109*, 12431−12442.
(63) Outka, D. A.; Madix, R. J. Broensted basicity of atomic oxygen on the gold(110) surface: reactions with methanol, acetylene, water, and ethylene. *J. Am. Chem. Soc.* **1987**, *109*, 1708−1714.
(64) Montoya, A.; Haynes, B. S. Methanol and Methoxide Decomposition on Silver. *J. Phys. Chem. C* **2007**, *111*, 9867−9876.
(65) Abild-Pedersen, F.; Greeley, J.; Studt, F.; Rossmeisl, J.; Munter, T. R.; Moses, P. G.; Skulason, E.; Bligaard, T.; Norskov, J. K. New Electromagnetic Mode in Graphene. *Phys. Rev. Lett.* **2007**, *99*. DOI: 10.1103/PhysRevLett.99.016105
(66) Bligaard, T.; Norskov, J. K.; Dahl, S.; Matthiesen, J.; Christensen, C. H.; Sehested, J. The Brønsted−Evans−Polanyi relation and the volcano curve in heterogeneous catalysis. *J. Catal.* **2004**, *224*, 206−217.
(67) Loffreda, D.; Delbecq, F.; Vigne, F.; Sautet, P. Fast Prediction of Selectivity in Heterogeneous Catalysis from Extended Brønsted-Evans-Polanyi Relations: A Theoretical Insight. *Angew. Chem., Int. Ed.* **2009**, *48*, 8978−8980.
(68) Zaffran, J.; Michel, C.; Auneau, F.; Delbecq, F.; Sautet, P. Linear Energy Relations As Predictive Tools for Polyalcohol Catalytic Reactivity. *ACS Catal.* **2014**, *4*, 464−468.
(69) Alcala, R.; Mavrikakis, M.; Dumesic, J. A. DFT studies for cleavage of C-C and C-O bonds in surface species derived from ethanol on Pt(111). *J. Catal.* **2003**, *218*, 178−190.
(70) Liu, B.; Greeley, J. Decomposition Pathways of Glycerol via C−H, O−H, and C−C Bond Scission on Pt(111): A Density Functional Theory Study. *J. Phys. Chem. C* **2011**, *115*, 19702−19709.
(71) Kresse, G.; Furthmuller, J. Efficient iterative schemes for *ab initio* total-energy calculations using a plane-wave basis set. *Phys. Rev. B: Condens. Matter Mater. Phys.* **1996**, *54*, 11169−11186.
(72) Kresse, G.; Furthmuller, J. Efficiency of ab-initio total energy calculations for metals and semiconductors using a plane-wave basis set. *Comput. Mater. Sci.* **1996**, *6*, 15−50.
(73) Perdew, J. P.; Wang, Y. Accurate and simple analytic representation of the electron-gas correlation energy. *Phys. Rev. B: Condens. Matter Mater. Phys.* **1992**, *45*, 13244−13249.
(74) Henkelman, G.; Uberuaga, B. P.; Jonsson, H. A climbing image nudged elastic band method for finding saddle points and minimum energy paths. *J. Chem. Phys.* **2000**, *113*, 9901−9904.
(75) Henkelman, G.; Jonsson, H. Improved tangent estimate in the nudged elastic band method for finding minimum energy paths and saddle points. *J. Chem. Phys.* **2000**, *113*, 9978−9985.
(76) Lausche, A. C.; Hummelshøj, J. S.; Abild-Pedersen, F.; Studt, F.; Nørskov, J. K. Application of a new informatics tool in heterogeneous catalysis: Analysis of methanol dehydrogenation on transition metal catalysts for the production of anhydrous formaldehyde. *J. Catal.* **2012**, *291*, 133−137.
(77) Chorkendorff, I.; Niemantverdriet, J. W. *Concepts of Modern Catalysis and Kinetics*, 2nd ed.; Wiley VCH: Weinheim, 2007.
(78) Vineyard, G. H. Frequency factors and isotope effects in solid state rate processes. *J. Phys. Chem. Solids* **1957**, *3*, 121−127.
(79) Kolasinski, K. W. *Surface Science: Foundations and Nanoscience*, 3rd ed.; Wiley: Chichester, UK, 2012.
(80) Campbell, C. T.; Arnadottir, L.; Sellers, J. R. V. Kinetic Prefactors of Reactions on Solid Surfaces. *Z. Phys. Chem.* **2013**, *227*, 1435−1454.
(81) Campbell, C. T.; Sellers, J. R. V. The Entropies of Adsorbed Molecules. *J. Am. Chem. Soc.* **2012**, *134*, 18109−18115.
(82) Greeley, J.; Mavrikakis, M. Methanol Decomposition on Cu(111): A DFT Study. *J. Catal.* **2002**, *208*, 291−300.
(83) Abild-Pedersen, F.; Andersson, M. P. CO adsorption energies on metals with correction for high coordination adsorption sites − A density functional study. *Surf. Sci.* **2007**, *601*, 1747−1753.

DOI: 10.1021/acs.jpcc.8b09415
J. Phys. Chem. C 2018, 122, 28158−28172